Acta Crystallographica Section D
Biological Crystallography
ISSN 0907-4449

Domain flexibility in the 1.75 Å resolution structure of Pb^{2+}-calmodulin

Mark A. Wilson[a] and Axel T. Brunger[b]*

[a]Rosenstiel Basic Medical Sciences Research Center, Brandeis University, 415 South Street, Waltham, MA 02453, USA, and [b]Howard Hughes Medical Institute and Department of Molecular and Cellular Physiology, James H. Clark Center Room E300-C, Stanford University, CA 94305, USA

Correspondence e-mail: axel.brunger@stanford.edu

Received 9 June 2003
Accepted 30 July 2003

PDB Reference: Pb^{2+}-calmodulin, 1n0y, r1n0ysf.

Calmodulin (CaM) regulates a variety of cellular processes by interacting with a large number of proteins in a Ca^{2+}-dependent manner. Conformational flexibility plays a key role in CaM function, although the full extent and detailed features of this flexibility are not fully characterized. Here, the 1.75 Å resolution crystal structure of Pb^{2+}-bound *Paramecium tetraurelia* CaM crystallized in a previously unobserved monoclinic lattice is reported. Pb^{2+}-CaM is disordered in this new lattice and only a portion of each of the two molecules in the asymmetric unit can be modeled. Comparison of the structures of Ca^{2+}-CaM and Pb^{2+}-CaM show close agreement in the C-terminal domain but significant structural differences in the N-terminal domain. In addition, translation–libration–screw (TLS) refinement and Rosenfield difference analysis reveal inter-helical flexibility in the metal-bound N-terminal domain of the protein that is absent in the metal-bound C-terminal domain and indicates that the two structurally similar domains of CaM are dynamically distinct. These results demonstrate that TLS refinement and Rosenfield difference analysis allow detailed information about macromolecular flexibility to be extracted from X-ray diffraction data even when the crystal lattice prohibits full manifestation of this flexibility.

1. Introduction

Calmodulin (CaM) is a small (148-amino-acid) highly conserved eukaryotic Ca^{2+}-binding protein of the EF-hand family that is centrally involved in the Ca^{2+} regulation of various signal transduction pathways. The Ca^{2+}-free and Ca^{2+}-bound forms of the protein interact with distinct classes of targets and each class is comprised of a surprisingly large and diverse array of proteins. The formation of a CaM–target complex alters the activity of the target protein, thereby indirectly conferring Ca^{2+} sensitivity to the target and the associated signalling pathway(s) (Chin & Means, 2000).

Structures of CaM in the Ca^{2+}-free (apo), Ca^{2+}-bound (holo) and various target-bound forms have been determined (Babu *et al.*, 1985; Kuboniwa *et al.*, 1995; Meador *et al.*, 1993). The protein consists of two structurally similar globular domains separated by a flexible ten-amino-acid linker region. Each globular domain consists of two helix–loop–helix (EF-hand) motifs related by approximate twofold symmetry and the loop portion of each EF-hand can coordinate a single Ca^{2+} with micromolar affinity. In the absence of Ca^{2+}, the helices that define the EF-hands are closely packed and oriented in an antiparallel fashion, constituting the compact closed form of the motif. Binding of Ca^{2+} causes the re-

orientation of the EF-hand helices to a more perpendicular orientation, resulting in a transition to the expanded open conformation of the motif (Zhang *et al.*, 1995). The Ca^{2+}-induced structural changes in CaM result in the solvent exposure of a hydrophobic cleft in each lobe and it is these solvent-exposed clefts that make direct contact with target proteins (Meador *et al.*, 1992). NMR (Chou *et al.*, 2001; Evenas *et al.*, 2001) and molecular-dynamics simulations (Barton *et al.*, 2002; Vigil *et al.*, 2001) have shown that the relative orientations of the EF-hand helices are subject to significant fluctuation and that the Ca^{2+}-bound N-terminal domain is more closed in solution than it is in the crystal. Therefore, although the time-averaged conformation of CaM changes significantly upon binding Ca^{2+}, this conformational change has an inherently dynamic character and is consequently more complex than a simple switch between two well defined conformations.

X-ray diffraction data are capable of providing detailed information about a subset of functionally relevant atomic displacements in CaM and other macromolecules. The influence of the direction and magnitude of atomic displacements on the observed X-ray diffraction data is usually described using the anisotropic displacement parameter (ADP). The ADP is a second-rank tensor that is equivalent (in one description) to the inverse of the variance–covariance matrix of the trivariate Gaussian probability density function for the position of the nucleus of each atom in the structure. Traditionally, data that extend to atomic ($d_{\min} < 1.2$ Å) resolution are required to provide an adequate observation-to-parameter ratio for refinement of the individual atomic ADPs, as the individual ADP description requires that six independent fit parameters per atom be added to the model. In order to refine ADPs against moderate-resolution (2.5–1.5 Å) data, the number of independent fit parameters must be reduced by assuming a physical model that introduces correlations amongst the ADPs. The most popular of these reduced-parameter ADP treatments is the translation–libration–screw (TLS) model of atomic displacements (Schomaker & Trueblood, 1966). This model assumes that all atoms within a user-specified group(s) constitute a rigid body and the displacements about the rigid-body degrees of freedom for this group(s) are refined to optimize the agreement between the model and the measured intensity data. In the most general case, each rigid group introduces 20 independent parameters to the refinement, which includes parameters that account for the correlation between translational and librational motion (Schomaker & Trueblood, 1966). Thus, for rigid groups of greater than three atoms, the TLS model contains fewer refined parameters than does the individual ADP model (six per atom). However, because Bragg diffraction data contain no direct information about correlated atomic displacements, the rigid-body assumption will always allow some component of non-rigid-body disorder to be absorbed into the refined TLS tensors. Consequently, the TLS result represents an upper limit for the contribution of true rigid-body disorder to the refined displacements and the physical validity of the resulting rigid-body description must always be viewed with caution.

Ca^{2+} is the physiologically relevant cation for CaM function; however, other cations can also bind to and activate CaM (Chao *et al.*, 1984). Of these, Pb^{2+} is of special interest because of the possible role that Pb^{2+}-CaM may play in Pb^{2+} toxicity (Goering, 1993; Goldstein, 1993). Pb^{2+} binds to all four metal-binding loops in CaM simultaneously and with such high affinity that Pb^{2+} can displace bound Ca^{2+} from CaM (Aramini *et al.*, 1996; Fullmer *et al.*, 1985). Furthermore, Pb^{2+} can functionally substitute for Ca^{2+} in some aspects of CaM function, including the ability of Pb^{2+}-CaM to bind to the target peptide from myosin light-chain kinase (Chao *et al.*, 1995).

Here, we report the 1.75 Å resolution crystal structure of Pb^{2+}-bound CaM. This is the first crystal structure of CaM bound to any metal other than Ca^{2+} and also the first structure of the target-free full-length wild-type protein in any space group other than *P*1. Pb^{2+}-CaM displays an unusual form of disorder in this new lattice, whereby only a portion of the two monomers in the asymmetric unit is ordered. Furthermore, a comparison of the crystal structures of Ca^{2+}-CaM and Pb^{2+}-CaM shows good agreement in the conformation of the C-terminal domain, but notable differences in the N-terminal domain. Lastly, both a TLS refinement of the displacement parameters in Pb^{2+}-CaM and a Rosenfield analysis of the ADPs from the atomic resolution structure of Ca^{2+}-CaM identify a pronounced flexing motion of the N-terminal domain that agrees with recent molecular-dynamics and NMR results and indicates that the two domains of metal-bound CaM are dynamically distinct.

2. Materials and methods

2.1. Sample preparation and crystallization

The expression clone for *Paramecium tetraurelia* CaM in the vector pKK233-3 (Amersham-Pharmacia) was a generous gift from the laboratory of C. Kung (University of Wisconsin-Madison, USA). CaM was overexpressed and purified as previously described (Putkey *et al.*, 1985). Lyophilized protein was resuspended in ultrapure water to a concentration of 15 mg ml^{-1} as determined spectrophotometrically using an extinction coefficient at 280 nm of 1280 M^{-1} cm^{-1}. Resuspended protein was brought to a final concentration of 5 m*M* $Pb(NO_3)_2$. Upon addition of Pb^{2+}, the solution became turbid with precipitated protein, which was partially clarified upon the addition of sodium acetate pH 4.0 to a final concentration of 100 m*M*. Sodium cacodylate pH 5.0 was then added to a final concentration of 50 m*M*. An ordered cacodylate ion was found to mediate an intermolecular interaction in the structure; if cacodylate was omitted, no crystals were obtained. Finally, the sample was titrated with 2-methyl-2,4-pentanediol (MPD) until the precipitate clarified, resulting in a final concentration of approximately 10% MPD. The sample was centrifuged at 16 000*g* and the supernatant was used for crystallization trials.

Hanging-drop vapor-diffusion crystallization trials were performed at 277 K by mixing 4 µl of the protein solution

Table 1
Data and model statistics.

Diffraction data	
Resolution (Å)	53–1.75 (1.81–1.75)
Space group	*C*2
Unit-cell parameters (Å, °)	a = 100.94, b = 30.79, c = 113.08, β = 109.3
Molecules per asymmetric unit	2
Unique reflections	33157
Completeness (%)	98.1 (94.7)
Multiplicity	5.4
$R_{\rm merge}$† (%)	11.0 (29.1)
$\langle I/\sigma(I)\rangle$	14.6 (4.1)
SAD phasing power	4.7 (3.3)
SAD figure of merit	0.78 (0.38)
Model statistics	
$R_{\rm work}$‡ (%)	21.4 (25.3)
$R_{\rm free}$§ (%)	22.3 (24.4)
No. of protein residues	165
No. of solvent atoms	149
No. of Pb^{2+}	14
Mean protein B factor (Å^2)	30.4
Mean bond-length deviations (Å)	0.007
Mean angle deviations (°)	1.219

† $R_{\rm merge} = \sum_{hkl}\sum_i |I^i_{hkl} - \langle I_{hkl}\rangle|/\sum_{hkl}\sum_i I^i_{hkl}$, where i is the ith observation of a reflection with index hkl and the angle brackets indicate an average over all i observations. ‡ $R_{\rm work} = \sum_{hkl} |F^C_{hkl} - F^O_{hkl}|/\sum_{hkl} F^O_{hkl}$, where F^C_{hkl} is the magnitude of the calculated structure factor with index hkl and F^O_{hkl} is the magnitude of the observed structure factor with index hkl. § $R_{\rm free}$ was calculated as $R_{\rm work}$, where the F^O_{hkl} were taken from a set of 3312 reflections (10% of the data) that were not included in the refinement.

(prepared as described above) and 4 µl of the reservoir solution (60–65% MPD, 50 m*M* sodium cacodylate pH 5.0). Clusters of rod-shaped crystals appeared after 2–10 d of equilibration and individual crystals typically measured 200 × 50 × 50 µm. The crystals were mechanically fragile and extremely sensitive to temperature fluctuations, so all work was performed in a cold room. The crystals were removed from the drop with a nylon loop and cooled by direct immersion in liquid propane, since the concentration of MPD in the mother liquor (60%) was sufficient to protect the crystals against freezing damage.

2.2. Data collection and processing

Single-wavelength anomalous diffraction (SAD) data were collected at beamline 9-1 at the Stanford Synchrotron Radiation Laboratory (SSRL) from a single crystal maintained at 100 K. The crystal was illuminated with 0.946 Å X-rays and data were collected using the oscillation method with a MAR345 image-plate detector (MAR Research, Evanston, IL, USA). The incident X-ray wavelength was chosen to be on the high-energy side of the Pb $L_{\rm III}$ edge, as an X-ray fluorescence scan could not be performed to determine which X-ray energy generated the maximum anomalous signal. The crystal belongs to space group *C*2 and contains two molecules in the asymmetric unit. Because the low symmetry of the space group makes radiation-induced deterioration of the anomalous signal a serious consideration, oscillation data were collected in 10° swaths, followed by the rotation of the crystal by 180° (*i.e.* inverse-beam mode), in order to collect Friedel mates as close in time as possible. The diffraction data were integrated in *DENZO* and scaled in *SCALEPACK* (Otwinowski & Minor, 1997), resulting in a 5.4-fold redundant 1.75 Å data set with an overall $R_{\rm merge}$ of 11.0%. The relatively high $R_{\rm merge}$ value is a characteristic feature of these crystals and does not reflect a particular problem with the crystal used in this study. See Table 1 for data statistics.

2.3. Structure solution and refinement

Ten of the 11 well ordered Pb^{2+} ions in the asymmetric unit were located using anomalous difference data in *SHELXD* (Usón & Sheldrick, 1999) and then input into *SHARP* (de La Fortelle & Bricogne, 1997) for maximum-likelihood heavy-atom parameter refinement and phase determination against the full range of the measured data (54–1.75 Å). Four of the 11 ordered Pb^{2+} sites were located in the EF-hand loops and the remaining seven were found to mediate a number of lattice contacts between the two molecules in the asymmetric unit. The quality of the final phase set was excellent, with a phasing power of 4.7 and a figure of merit of 0.78 over all acentric reflections (Table 1). Density modification (solvent flipping and density truncation) in *SOLOMON* (Abrahams & Leslie, 1996) improved the appearance of the electron density, but maps calculated using the initial experimental phases were readily interpretable prior to modification (Fig. 1).

The structure was manually built into the density-modified electron-density maps using *O* (Jones *et al.*, 1991) and was initially refined in *CNS* (Brünger *et al.*, 1998). The asymmetric unit contains two molecules of Pb^{2+}-CaM, with the N-terminal domain of molecule *A* and the C-terminal domain of molecule *B* being well ordered. There is weak electron density for some of the disordered regions of the two molecules, but it is not interpretable and was left unmodeled (see §3). Refinement of the manually built model was performed against a maximum-likelihood target that incorporated experimental phase information *via* the inclusion of Hendrikson–Lattman coefficients (Hendrickson & Lattman, 1970; MLHL target) and used structure-factor amplitudes that did not contain any anomalous scattering contribution. No σ cutoff was applied to the measured data and a bulk-solvent correction and anisotropic scaling of the data was performed. Initial simulated-annealing torsion-angle refinement (Rice & Brünger, 1994) was followed by alternating cycles of manual model adjustments in *O* (Jones *et al.*, 1991) and conjugate-direction refinement of coordinates and individual isotropic B factors. At this stage, strong negative difference density was noted on the Pb^{2+} ion bound to site III in $mF_o - DF_c$ maps, indicating that this Pb^{2+} ion was not fully occupied. Consequently, the occupancies of the Pb^{2+} ion were refined for ten cycles and subsequently fixed. The final cycles of refinement were performed against a maximum-likelihood target based on amplitudes alone (MLF), as this resulted in a significant decrease in the $R_{\rm free}$ value compared with identical refinements against the MLHL target. Nearly all of this difference appears to be a consequence of the B-factor refinement, as there were no significant coordinate shifts between the MLHL and MLF refinements, but the B factors differ considerably. The final *CNS* model was further refined in *REFMAC*5

(Murshudov *et al.*, 1997) using the TLS model described below. The final model had excellent stereochemistry and Ramachandran quality, with 95.3% of residues in core regions and 4.7% of the residues in allowed regions. No residues were located in disallowed regions. See Table 1 for final model statistics.

2.4. TLS model refinement and analysis

All TLS refinements were performed in *REFMAC*5 (Murshudov *et al.*, 1997; Winn *et al.*, 2001). Three refinements differing only in the definition of the rigid groups were performed in order to determine which model provided the best agreement with the diffraction data. Model 1 consisted of a single rigid group comprising all of the protein atoms and ordered Pb^{2+} ions in the asymmetric unit. Model 2 treated each of the two monomers in the asymmetric unit as separate rigid groups, with residues 1–87 (molecule *A*) and Pb^{2+} 500–504 as the first group, and residues 69–147 (molecule *B*) and Pb^{2+} 505–510 as the second rigid group. Model 3 contained three rigid groups: residues 1–17, 63–87 (molecule *A*) and Pb^{2+} 502 and 504 in the first group, residues 18–62 (molecule *A*) and Pb^{2+} 500, 501 and 503 in the second group, and residues 69–147 (molecule *B*) and Pb^{2+} 505–510 in the third rigid group. Model 3 corresponds to a partitioning of the N-terminal domain into two groups, where the choice of rigid groups was based on the results of a *DYNDOM* (Hayward & Berendsen, 1998) comparison of the fully open crystalline form of the domain and the more closed solution structure (PDB code 1j70; Chou *et al.*, 2001). The *DYNDOM* result identified a pronounced hinge-bending motion that related these two structures and provided information about the location of the putative hinge region that was subsequently used to divide the domain for the TLS refinement. Pb^{2+} ions were included in the various TLS groups because these electron-dense scatterers contribute heavily to the observed intensities, particularly at higher resolution, and there are extensive interactions between the protein and the Pb^{2+} ions in this structure.

All TLS refinements were performed using the same starting coordinates and with all isotropic *B* factors set to 25 Å^2 (Winn *et al.*, 2001). The rigid-body origin for the calculations was set to the center of mass of the rigid group and was not refined. However, the screw tensor was allowed to be non-symmetric in order to account for the fact that the center of mass will not, in general, correspond to the true center of reaction for the rigid group. Both side-chain and main-chain atoms were included in the rigid groups and TLS refinements were carried out for 20 cycles of conjugate-gradient least-squares refinement against all measured data using an amplitude-based maximum-likelihood target function. A bulk-solvent model was employed to allow the inclusion of the low-resolution ($d_{\min} > 6$ Å) data and an overall anisotropic scale factor was applied. After the TLS refinement was complete, an additional 20 cycles of restrained conjugate-gradient least-squares minimization of both coordinates and isotropic *B* factors were performed. The same set of reflections were sequestered and used for the calculation of $R_{\rm free}$ (Brünger, 1992) throughout the *CNS* and *REFMAC*5 portions of the refinement. The resulting tensors were analyzed and used to calculate individual ADPs using *TLSANL* (Howlin *et al.*, 1993).

2.5. Rosenfield analysis of Ca^{2+}-CaM

Rosenfield analysis was performed on the ADPs from the 1.0 Å structure of Ca^{2+}-CaM (Wilson & Brunger, 2000; PDB code 1exr) using *ANISOANL* (Rosenfield *et al.*, 1978). Only main-chain atoms were used in the calculation of the difference values and the results were averaged in bins of approximately five residues. This reduced noise in the matrix and consequently allowed systematic trends in the difference values to be observed more easily.

2.6. Solvent-accessible surface area and inter-helical angle calculations

Solvent-accessible surface areas were calculated in *CNS* using residues 6–75 of the N-terminal domain of CaM. Inter-helical angles were calculated using *INTERHLX* (courtesy of K. Yap, University of Toronto, Canada) and converted to the values shown in Table 2 by subtraction from 180°.

3. Results

3.1. Disorder in Pb^{2+}-CaM

Inspection of experimentally phased electron-density maps indicates that only a portion of each of the two molecules present in the asymmetric unit is ordered. The two molecules are related by a non-crystallographic twofold symmetry operation, with the N-terminal domain of molecule *A* and the C-terminal domain of molecule *B* being ordered. Throughout the paper, molecule *A* will designate the ordered N-terminal domain (residues 1–87) of the first molecule in the asymmetric unit and molecule *B* will designate the ordered C-terminal domain (residues 69–147) of the second molecule in the asymmetric unit. As shown in Fig. 2, the disordered portions of these two molecules are adjacent, which results in an unusual lattice with alternating layers of well ordered and poorly ordered domains. This peculiar packing arrangement may explain the acute sensitivity of these crystals to temperature fluctuations and mechanical stress, and demonstrates that the structure of Pb^{2+}-CaM is highly flexible, even within the constrained environment of the crystal.

Because there is no interpretable electron density in the disordered regions of the two molecules, the physical nature of the conformational disorder cannot be determined with certainty. There are at least two plausible explanations. Firstly, flexibility of the central helix may allow substantial rigid-body domain displacements, thereby smearing out the electron density for the most mobile regions of the protein. Secondly, flexibility of the individual domains may result in extreme conformational heterogeneity that renders the electron density in these regions uninterpretable. Conclusively establishing which of these possibilities is responsible for the observed disorder will require information about the corre-

lation length of the structural disorder, as could be provided by analysis of the pronounced diffuse scattering that was observed from these crystals. This was not performed here because of the many difficulties inherent in the collection, integration and interpretation of diffuse scattering data (Wall *et al.*, 1997).

Table 2
Comparison of inter-helical angles in the N-terminal domain of CaM.

Inter-helical angles were calculated using *INTERHLX* (courtesy of K. Yap, University of Toronto, Canada) and converted to the values shown by subtraction from 180°.

	A–*B* angle (°)	*C*–*D* angle (°)	PDB code
Ca^{2+}-CaM crystal	91	95	1exr
Ca^{2+}-CaM solution	76	79	1j7o
Ce^{3+}-CaM solution	89	87	1ak8
Pb^{2+}-CaM crystal	85	104	1n0y

In lieu of this information, several pertinent observations can still be made. Firstly, the voids in the lattice resulting from the disordered (and hence unmodeled) regions of the protein are large enough to accommodate both missing domains in the same conformation as in the ordered portion of the structure without unreasonably close contacts. Secondly, after the initial model of the ordered portion of the asymmetric unit was refined, several prominent peaks in $mF_o - DF_c$ electron-density maps were located very near to the metal-binding loops in the disordered regions of molecules *A* and *B*, indicating that Pb^{2+} is bound to these domains. The difference electron density for the putative Pb^{2+} sites is highly anisotropic and shows evidence of discrete disorder, suggesting a high degree of mobility. Thirdly, the molar ratio of Pb^{2+} to CaM in the drop is 5.5:1, almost exactly equal to the ratio of well ordered Pb^{2+} sites (excluding the sites in the disordered region) to CaM seen in the crystal. Taken together, these

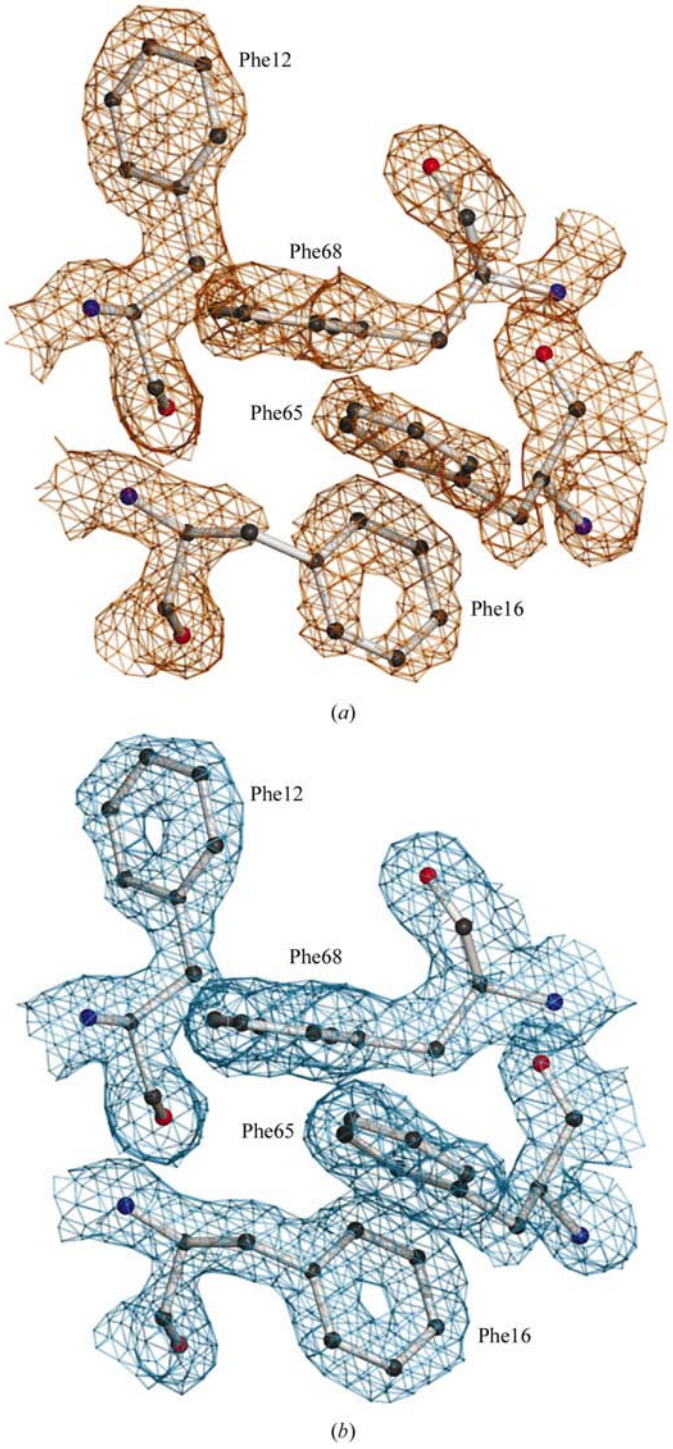

Figure 1
Electron density for a cluster of phenylalanines in the N-terminal binding pocket. In (*a*), the electron density is calculated from density-modified SAD phases and reveals the generally high quality of the initial electron-density map. In (*b*), the final $2mF_o - DF_c$ electron-density map is shown for comparison. This figure was produced using *POVscript+* (Fenn *et al.*, 2003).

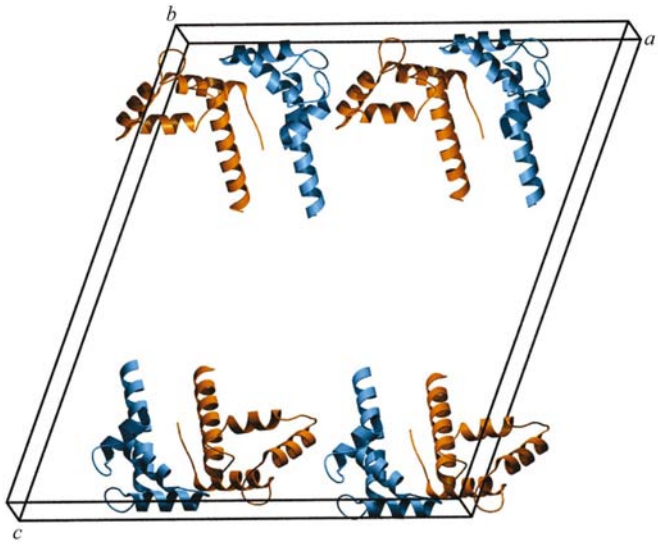

Figure 2
A view of the unit cell. The ordered portions of the unit cell are shown, with the N-terminal domain (molecule *A*) in orange and the C-terminal domain (molecule *B*) in blue. The void in the middle of the cell is large enough to accommodate the remainder of the two molecules and the resulting lattice contains alternating well ordered and poorly ordered layers. This figure was produced using *POVscript+* (Fenn *et al.*, 2003).

observations suggest that the disordered domains may not be fully saturated with Pb^{2+} and that the resulting conformational heterogeneity is the source of the extreme disorder in this region of the molecule. This does not exclude the possibility of an additional contribution from quasi-rigid-body domain displacements.

3.2. Structural comparison of Ca^{2+}-CaM and Pb^{2+}-CaM

A least-squares superposition of the ordered portions of Pb^{2+}-bound CaM on the corresponding regions of Ca^{2+}-CaM (PDB code 1exr) reveals that the N-terminal domains (molecule *A* of Pb^{2+}-CaM) are significantly different, with a C^{α} root-mean-squared deviation (r.m.s.d.) of 2.1 Å (residues 2–87). In contrast, the C-terminal domains (molecule *B* of Pb^{2+}-CaM) compare more favorably, with a C^{α} r.m.s.d. of 1.1 Å (residues 69–147). The N-terminal domains of Pb^{2+}-CaM and Ca^{2+}-CaM exhibit the largest discrepancies in the N-terminal seven residues of helix *A* and the C-terminal half of helix *D*/*E*, while the differences in the C-terminal domains are smaller and confined principally to the loop connecting helices *F* and *G* (Fig. 3). Flexibility in the C-terminal loop has been observed in the crystal structure of the isolated Ca^{2+}-bound C-terminal domain (Olsson & Sjolin, 2001) and has also been inferred on the basis of characteristically low-order parameters and high ensemble conformational variability in NMR models (Finn *et al.*, 1995).

The Pb^{2+} ion bound to site III in the C-terminal domain refined to a low occupancy of 0.3, while all other Pb^{2+} sites had refined occupancies near unity. In all four metal-binding loops of CaM, the Pb^{2+} coordination is essentially identical to that of Ca^{2+}, including the seventh water ligand to the metal ion. Despite the low occupancy of the Pb^{2+} in site III, the structure of the C-terminal domain of Pb^{2+}-CaM is very similar to that of fully saturated Ca^{2+}-CaM. Given that the Pb^{2+} sites in the N-terminal domain are both fully occupied and display identical coordination geometry in comparison to Ca^{2+}, the structural differences observed the N-terminal domains of Pb^{2+}-CaM and Ca^{2+}-CaM cannot arise from altered metal-coordination geometry or partial metal occupancy. Also, the qualitative similarity of disorder in the N-terminal domains of Pb^{2+}-CaM and Ca^{2+}-CaM strongly suggests that this flexibility is an intrinsic property of the protein and not an effect specific to Pb^{2+}-CaM (see below).

The N-terminal seven residues of molecule *A* participate in extensive Pb^{2+}-mediated crystal contacts with symmetry-related molecules, explaining the large differences in conformation between this portion of Pb^{2+}-CaM and Ca^{2+}-CaM shown in Fig. 3. The differences in the orientation of helix *D*/*E*, however, cannot be easily rationalized on the basis of observed lattice contacts. It is possible that some aspect of the conformation or packing of the disordered C-terminal portion of molecule *A* favors the reorientation of helix *D*/*E* observed here. A comparison of the inter-helical angles of the N-terminal domains (residues 6–75) of the solution structures of Ca^{2+}-CaM and Ce^{3+}-CaM (PDB code 1ak8; Bentrop *et al.*, 1997) and the crystal structures of Ca^{2+}-CaM and Pb^{2+}-CaM is shown in Table 2. Both pairs of inter-helical angles (between helices *A*–*B* and *C*–*D*) in Pb^{2+}-CaM differ from other structures of the metal-bound N-terminal domain of CaM; however, the total solvent-accessible surface area of the N-terminal domain (residues 6–75) is only 180 $Å^2$ smaller in Pb^{2+}-CaM than in Ca^{2+}-CaM. Thus, it appears that the contraction of the *A*–*B* inter-helical angle and the expansion of the *C*–*D* inter-helical angle are compensatory and do not greatly alter the total solvent-accessible surface area of the domain.

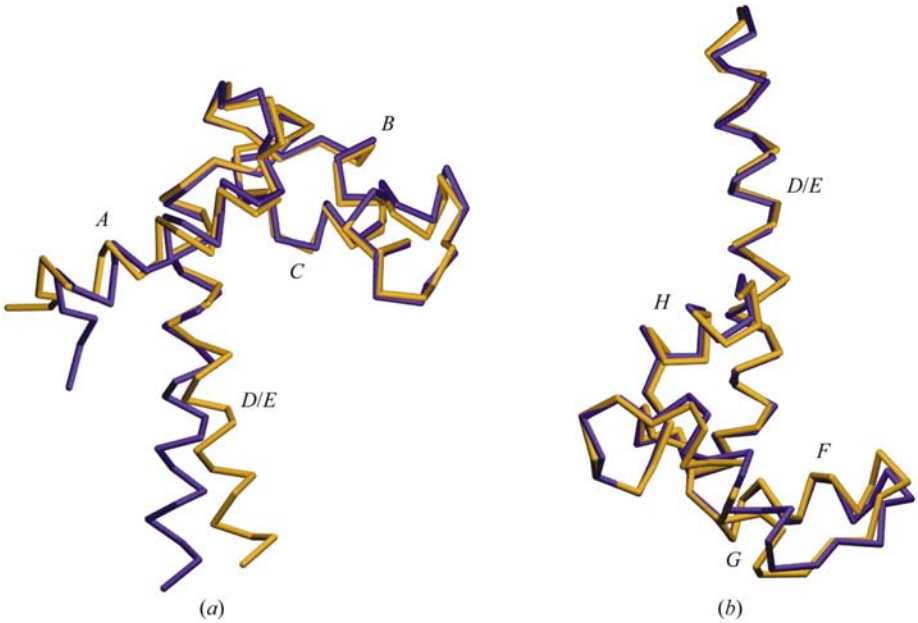

Figure 3
Least-squares superposition of Pb^{2+}-CaM and Ca^{2+}-CaM. In (*a*), molecule *A* of Pb^{2+}-CaM (blue) and the corresponding region of Ca^{2+}-CaM (gold) are shown. Significant deviations are apparent in the orientation of helix *D*/*E* (at the bottom of the figure) with the rest of the molecule. In (*b*), molecule *B* of Pb^{2+}-CaM (blue) and the corresponding region of Ca^{2+}-CaM (gold) are shown, illustrating the generally better agreement between the Pb^{2+}-CaM and Ca^{2+}-CaM structures in this region of the molecule. This figure was produced using *POVscript+* (Fenn *et al.*, 2003).

3.3. Identification of a domain-closure motion in the N-terminal domain

A comparison of the *B* factors from the 1.0 Å crystal structure of Ca^{2+}-CaM and Pb^{2+}-CaM reveals that although the C-terminal domains are comparable, there are major variations in the N-terminal domains (Fig. 4). In particular, residues 30–65 show substantially elevated *B* factors in the Pb^{2+}-bound structure, which are not seen in Ca^{2+}-CaM. As shown at the bottom of Fig. 4, these residues comprise helices *B* and *C* and the delimiting residues (30 and 65) are near the metal-binding

loops. It should be noted that there are few direct crystal-packing contacts in the vicinity of this loop (Fig. 2), in contrast to the many direct crystal-packing interactions that occur in this region of the triclinic Ca^{2+}-CaM structure. The smaller number of constraining interactions with the lattice may explain why this region of the Pb^{2+}-CaM N-terminal domain is more flexible than the corresponding region of Ca^{2+}-CaM.

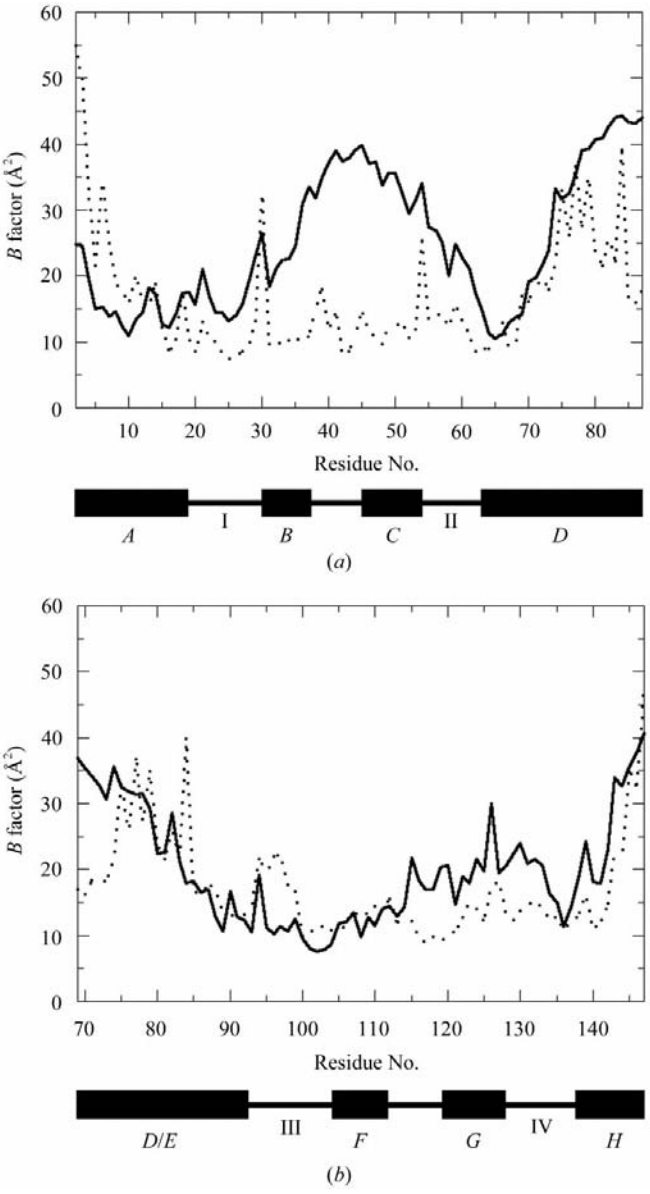

Figure 4
A comparison of residue-averaged isotropic *B* factors from Pb^{2+}-CaM (solid line) and Ca^{2+}-CaM (dotted line). The N-terminal domain (molecule *A*) is shown in (*a*) and the C-terminal domain (molecule *B*) in (*b*). The secondary structure is illustrated below each plot, with large black boxes corresponding to helices (labeled *A*–*H*) and thin lines corresponding to loops. The metal-binding loops are labeled I–IV. In (*a*), the *B* factors in the helix *B*–*C* region of molecule *A* of Pb^{2+}-CaM are clearly elevated compared with the corresponding region of Ca^{2+}-CaM, reflecting the greater mobility of the N-terminal domain of Pb^{2+}-CaM in a monoclinic lattice. In (*b*), the *B* factors in the C-terminal domain compare favorably, with no striking discrepancies between Pb^{2+}-CaM and Ca^{2+}-CaM.

Table 3
Comparison of various TLS models.

Model	TLS groups	Isotropic *B* factors	R_{free} (%)	R_{work} (%)	Anisotropy†	Residual *B*-factor r.m.s.d.‡ (Å^2)
Isotropic	0	25 Å^2 fixed	32.8	32.4	—	—
		Refined	23.8	22.9	1	1.39
1	1	25 Å^2 fixed	27.4	26.7	—	—
		Refined	22.8	21.9	0.45	1.39
2	2	25 Å^2 fixed	26.6	25.9	—	—
		Refined	22.6	21.5	0.38	1.34
3	3	25 Å^2 fixed	26.0	25.4	—	—
		Refined	22.3	21.4	0.36	1.29

† Anisotropy is defined as the ratio of the smallest to largest eigenvalues of the ADP tensor and the values above include only the contribution of protein atoms. Anisotropy was calculated using *PARVATI* (Merritt, 1999). The residual *B* factors represent the component of the molecular disorder that is not described by the TLS model.

While the elevated *B* factors in the helix *B*–*C* regions of the Pb^{2+}-bound N-terminal domain clearly indicate that these two helices are mobile, information about the preferred direction of displacement of this region is required to determine the type of motion that helices *B* and *C* execute with respect to helices *A* and *D*. Because the resolution of the data (1.75 Å) is too low to allow the refinement of individual ADPs, the TLS model was employed.

Three different TLS models of Pb^{2+}-CaM were tested: the first in which both molecules *A* and *B* and the bound Pb^{2+} in the asymmetric unit were treated as a single group (model 1), the second in which the two molecules and their associated Pb^{2+} were treated as two separate groups (model 2) and the third in which three groups comprising helices *A* and *D* (residues 1–17 and 63–87), helices *B* and *C* (residues 18–62) and all of molecule *B* (residues 69–147) were treated as separate groups (model 3). The partitioning of the N-terminal domain of molecule *A* in model 3 is based on both the elevated *B* factors of the helix *B*–*C* region, which suggests that this portion of the domain may move relative to the helices *A* and *D*, and the results of a comparison of the semi-closed NMR structure of the N-terminal domain (Chou *et al.*, 2001) and the structure of the more open crystal structure (see §2).

The TLS models were initially refined with all isotropic *B* factors fixed at 25 Å^2 in order to minimize bias in the refined TLS tensors (Winn *et al.*, 2001). After TLS refinement was complete, the isotropic *B* factors were refined (see §2). These refined isotropic *B* factors represent the residual internal motion of the quasi-rigid groups that cannot be adequately described by the TLS model, as well as containing contributions from various sources of error. All of the TLS models represent an improvement over the individual isotropic *B*-factor model, but model 3 provides the best fit to the data as judged by the R_{free} value both before and after the contribution of residual non-rigid-body motion was included *via* *B*-factor refinement (Table 3). Furthermore, the distribution of residual isotropic *B* factors is more uniform in model 3 than in either model 1 or 2 (Table 3), indicating that the TLS treatment in model 3 provides a more complete description of the total molecular displacement than do either models 1 or 2. Consequently, model 3 is the subject of all subsequent analysis.

Table 4
TLS tensor eigenvalues for model 3.

Residues in TLS groups	T eigenvalues (Å^2)	L eigenvalues ($^{\circ 2}$)	S eigenvalues† (Å $^\circ$)
Group 1 (1–17, 63–87)	−0.037	3.445	0.281
	0.070	15.393	−0.048
	0.013	−0.975	−0.233
Group 2 (18–62)	0.014	11.733	0.390
	−0.011	2.575	−0.120
	0.061	3.339	−0.270
Group 3 (69–147)	−0.012	0.387	0.204
	0.063	3.499	−0.174
	0.015	1.012	−0.031

† The S tensor eigenvalues were calculated from the symmetrized S tensor. S was made symmetric by referring it to a coordinate system whose origin is at the center of reaction for the rigid group.

Inspection of the libration tensor eigenvalues in Table 4 shows that the librations of the two TLS groups comprising the N-terminal domain are large and anisotropic, with both groups possessing highly dominant libration axes. As shown in Fig. 5, the dominant non-intersecting screw axes (which contain information about both the librational components of the motion and translation–libration correlation) for these two N-terminal groups indicate a complex composite motion that can be roughly described as a shearing opening–closing motion of the N-terminal domain. The ADPs calculated from the TLS parameters are shown in Fig. 5(*b*) for comparison. This pronounced lobe-closure motion in the N-terminal domain of molecule *A* is notably absent in the C-terminal domain of molecule *B*, which, based on the more uniform distribution of isotropic *B* factors throughout the domain, appears to behave more like a single quasi-rigid body without substantial relative motions of its constituent helices.

3.4. Comparison with anisotropic disorder in the N-terminal domain of Ca^{2+}-CaM

Further evidence in support of the view that the metal-bound N-terminal domain is more internally flexible than the metal-bound C-terminal domain is provided by a Rosenfield analysis of the ADPs from the 1.0 Å structure of Ca^{2+}-bound CaM (Wilson & Brunger, 2000). Rosenfield analysis determines the difference in the projection of the ADPs of a pair of atoms along a line that joins the two atoms. Small difference values indicate that the two atoms display a high degree of correlation in the spatial properties of their displacements, consistent with (but not conclusively establishing) rigid-body motion. In contrast, large difference values indicate that the two atoms are not likely to belong to the same rigid group, thereby implying the existence of internal modes of flexibility within the portion of the protein containing these two atoms (Rosenfield *et al.*, 1978).

The Rosenfield matrices for the N- and C-terminal domains of 1exr are shown in Fig. 6. The C-terminal domain shows relatively small and uniform difference values for the main-chain atoms (excepting the flexible C-terminal residues), suggesting that there is little relative displacement of the helices in this domain. In contrast, the N-terminal domain shows several regions of elevated difference values, especially between helices *A* and *C* and *B* and *D*, indicating that this domain contains a substantial amount of inter-helical flexibility. Moreover, the Rosenfield matrix for the N-terminal domain of Ca^{2+}-CaM and the TLS result for Pb^{2+}-CaM agree, both indicating that helices *A* and *D* and *B* and *C* constitute a pair of quasi-rigid groups that move relative to one another.

4. Discussion

4.1. Structural effects of Pb^{2+} substitution in CaM

The overall conformation and metal-coordination geometry of Pb^{2+}-CaM is similar to that of Ca^{2+}-CaM, thus providing a structural rationale for the ability of Pb^{2+}-CaM to bind to and activate some of the same targets as Ca^{2+}-CaM (Chao *et al.*, 1995). However, unlike Ca^{2+} in previous triclinic structures, Pb^{2+} is found to mediate a large number of lattice contacts in this structure. Of the 11 well ordered Pb^{2+} sites, only four are in the metal-binding loops of CaM, with the remainder concentrated at the interface of molecules *A* and *B*. In particular, the combined influence of Pb^{2+}-mediated crystal contacts and inherent structural plasticity is the probable cause of the differences in the conformation of the N-terminal domains of Ca^{2+}-CaM and Pb^{2+}-CaM (see §3). Furthermore, the large number of Pb^{2+}-mediated contacts between molecules *A* and *B* observed in this new monoclinic lattice is likely to be the reason why Pb^{2+}-CaM crystallizes in a different space group to Ca^{2+}-CaM. It is not clear why Pb^{2+} seems more prone to form intermolecular salt bridges than Ca^{2+} in CaM crystal structures, although the differing crystallization conditions of Ca^{2+}-CaM and Pb^{2+}-CaM may be responsible.

4.2. Dynamic asymmetry in the two domains of CaM

The conformation of the N-terminal domain of Pb^{2+}-CaM is found to differ from previous Ca^{2+}-CaM structures solved in triclinic lattices, while the C-terminal domain compares favorably with previous crystal structures of Ca^{2+}-CaM. Recent NMR (Chou *et al.*, 2001) and solution X-ray scattering (Vigil *et al.*, 2001) studies have found that the solution conformation of the N-terminal domain of Ca^{2+}-CaM is more closed than observed in previous crystal structures. Because crystallization of CaM requires conditions that are markedly different from those used in the solution-scattering and NMR experiments, it is unclear whether the discrepancies between the solution and crystal structures arise from crystal-packing forces selecting an open conformation of the N-terminal domain or are a consequence of differing solution conditions altering the conformational preferences of the protein. Irrespective of the physical cause of the differences, the fact that the solution and crystal structures of the N-terminal domain differ so significantly while the C-terminal domains agree more closely indicates that the conformation of the metal-bound N-terminal domain is subject to significantly greater fluctuation than is the C-terminal domain.

In addition to evidence from structure comparisons, displacement-parameter analysis also indicates that the metal-

bound N-terminal domain has a greater degree of internal flexibility than does the C-terminal domain. In particular, helices *B* and *C* are more mobile in this structure than in previous triclinic structures of Ca^{2+}-CaM and TLS refinement identifies a domain-closure motion in the N-terminal domain that is in qualitative agreement with the result of a Rosenfield analysis of the ADPs in Ca^{2+}-CaM. It is important to note that the consistency of the TLS refinement of Pb^{2+}-CaM and the Rosenfield analysis of Ca^{2+}-

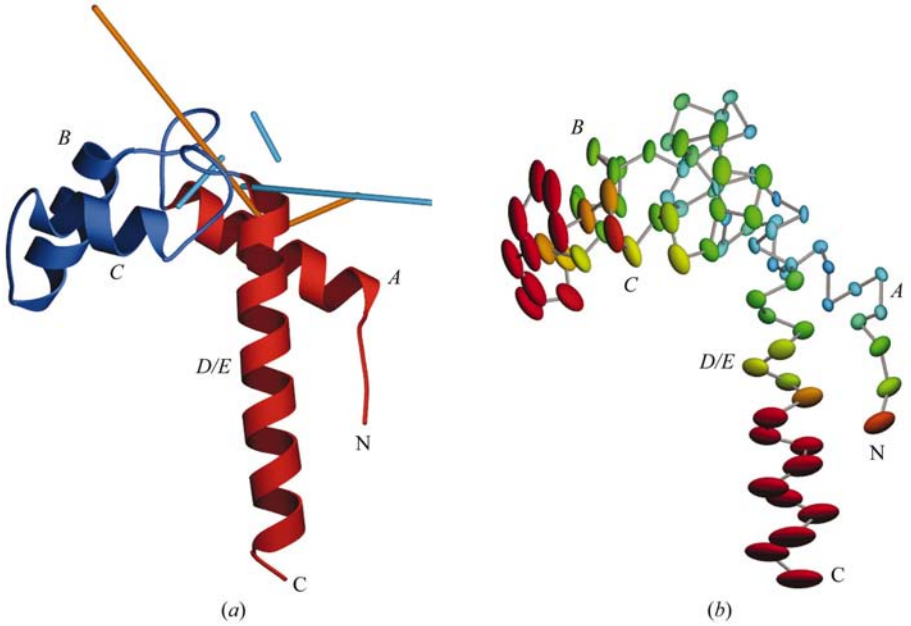

Figure 5
The TLS model of anisotropic flexibility in molecule *A* of Pb^{2+}-CaM. In (*a*), the non-intersecting screw axes resulting from TLS refinement are shown superimposed on the ribbon diagram of molecule *A*. The two rigid groups and their corresponding screw axes are colored red (helices *A* and *D*/*E*) and blue (helices *B* and *C*). For both groups, there is a highly dominant screw axis and the resulting motion is a shearing opening–closing motion of the domain. In (*b*), the C^{α} ADPs calculated from the TLS model are shown colored according to the magnitude of the displacements, ranging from blue (smallest) to red (largest). The opening–closing motion of the domain is apparent from the large and highly anisotropic displacements of helices *B*–*C* and helix *D*/*E*. This figure was produced using *POVscript+* (Fenn *et al.*, 2003).

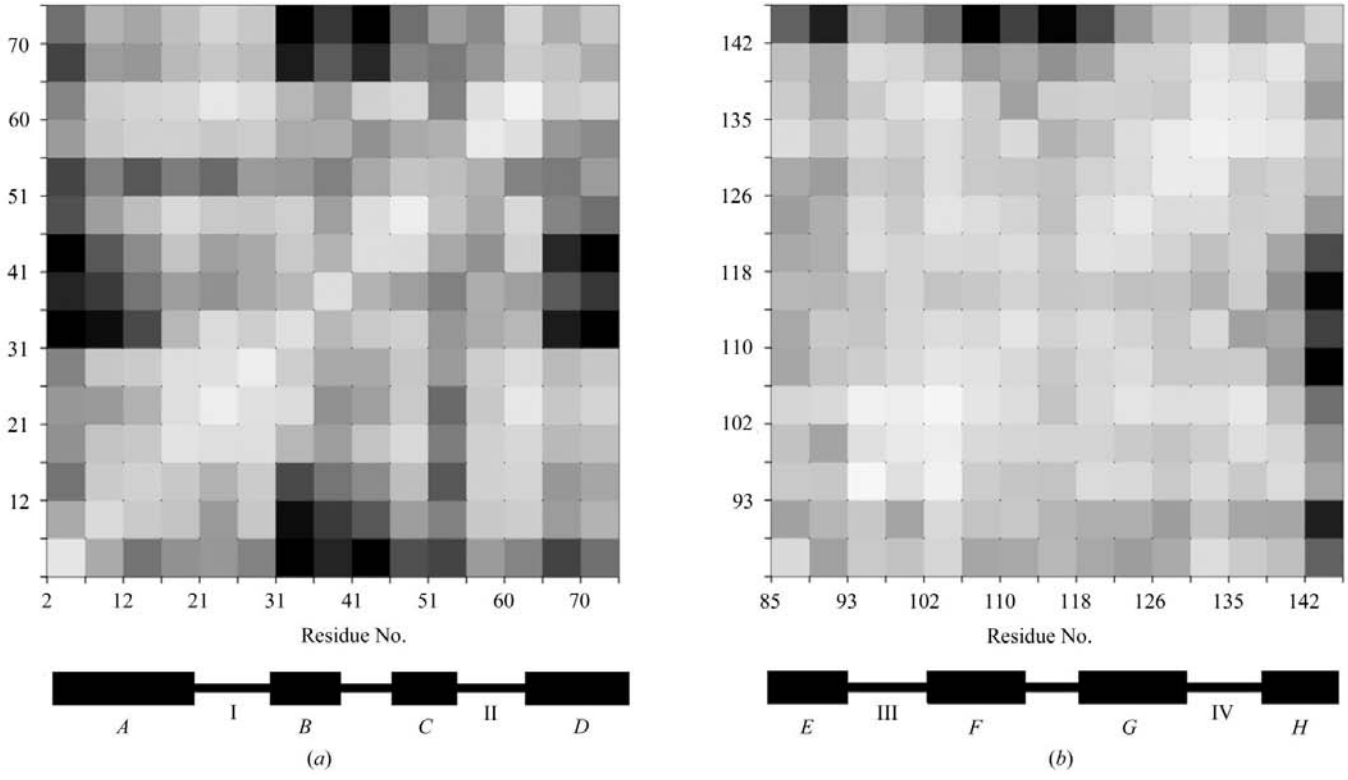

Figure 6
Rosenfield matrices for the ADPs in Ca^{2+}-CaM. The difference values for ADPs of main-chain atoms are displayed, with larger difference values corresponding to darker boxes. For clarity, the difference values are averaged in bins of approximately five residues. Below each matrix, the secondary structure is illustrated, with black boxes corresponding to helices (labeled *A*–*H*) and black lines corresponding to loops. Metal-binding loops are labeled I–IV. In (*a*), the Rosenfield matrix for the N-terminal domain is shown. The main-chain ADPs of helices *A* and *C* and *B* and *D* differ considerably, in agreement with the TLS analysis and indicating substantial inter-helical flexibility in the N-terminal domain. In (*b*), the C-terminal difference values are shown, revealing smaller and more uniform difference values than are seen in the N-terminal domain. This is consistent with the absence of appreciable inter-helical motion in the C-terminal domain. The largest difference values in this domain are observed for the terminal residues, which are expected to be more flexible. This figure was produced with *ANISOANL*.

CaM indicates that the presence of inter-helical flexibility of the N-terminal domain is an intrinsic property of the metal-bound form of the domain and is not a response to the specific metal bound to the protein. However, because the structures of Pb^{2+}-CaM and Ca^{2+}-CaM differ both in the identity of the bound metal and the space group, it cannot be conclusively established based on this work alone whether the large-amplitude inter-helical disorder observed for Pb^{2+}-CaM is an effect specific to Pb^{2+}-CaM or is common to both Pb^{2+}-CaM and Ca^{2+}-CaM. We favor the latter hypothesis because the Pb^{2+}-CaM crystal-packing contacts in this monoclinic cell are less restrictive to motion of helices *B* and *C* than in triclinic Ca^{2+}-CaM, allowing the inherent mobility of this domain to be more fully manifested in this new monoclinic cell.

These results indicate that the two structurally similar domains of CaM are dynamically distinct, with the metal-bound N-terminal domain possessing significantly more inter-helical flexibility than the metal-bound C-terminal domain. NMR studies have shown that this situation is reversed in metal-free CaM, where the C-terminal domain samples both closed and open conformations on the microsecond timescale, while the metal-free N-terminal domain shows no evidence of conformational exchange on comparable timescales (Evenas *et al.*, 2001; Malmendal *et al.*, 1999; Tjandra *et al.*, 1995). Therefore, not only do the two domains of CaM appear to possess different internal dynamics, but the nature and extent of the motions appears to be sensitive to the presence of metals in the EF-hand loops. This is supported by the detailed view of CaM dynamics afforded by molecular-dynamics simulations. In particular, Vigil and coworkers identified an opening–closing motion in the N-terminal domain of Ca^{2+}-CaM that qualitatively agrees with the results of the TLS refinement presented here (Vigil *et al.*, 2001). Furthermore, this simulation showed no evidence of a similar flexing motion in the Ca^{2+}-bound C-terminal domain, in agreement with a more recent simulation study of the isolated domains of Ca^{2+}-free and Ca^{2+}-loaded CaM (Barton *et al.*, 2002).

5. Conclusions

The qualitative agreement between the crystallographic, spectroscopic and simulation views of CaM mobility discussed here indicates that atomic displacement parameters contain detailed information about molecular flexibility that can be extracted from even moderate-resolution data using modern refinement protocols. Furthermore, it suggests that although protein mobility is limited in the crystalline environment, lattice constraints do not appear to alter the fundamental spatial characteristics of protein flexibility. This observation should prove valuable in correlating the results of solution and crystallographic studies of protein dynamics.

We thank Luke Rice for assistance with data collection, Carolyn Cohen and Tim Fenn for critical reading of the manuscript and Kyoko Yap for providing us with her program *INTERHLX*. Portions of this research were carried out at the Stanford Synchrotron Radiation Laboratory, a national user facility operated by Stanford University on behalf of the US Department of Energy, Office of Basic Energy Sciences. The SSRL Structural Molecular Biology Program is supported by the Department of Energy, Office of Biological and Environmental Research and by the National Institutes of Health, National Center for Research Resources, Biomedical Technology Program and the National Institute of General Medical Sciences.

References

Abrahams, J. P. & Leslie, A. G. W. (1996). *Acta Cryst.* D**52**, 30–42.
Aramini, J. M., Hiraoki, T., Yazawa, M., Yuan, T., Zhang, M. J. & Vogel, H. J. (1996). *J. Biol. Inorg. Chem.* **1**, 39–48.
Babu, Y. S., Sack, J. S., Greenhough, T. J., Bugg, C. E., Means, A. R. & Cook, W. J. (1985). *Nature (London)*, **315**, 37–40.
Barton, N. P., Verma, C. S. & Caves, L. S. A. (2002). *J. Phys. Chem. B*, **106**, 11036–11040.
Bentrop, D., Bertini, I., Cremonini, M. A., Forsen, S., Luchinat, C. & Malmendal, A. (1997). *Biochemistry*, **36**, 11605–11618.
Brünger, A. T. (1992). *Nature (London)*, **355**, 472–475.
Brünger, A. T., Adams, P. D., Clore, G. M., DeLano, W. L., Gros, P., Grosse-Kunstleve, R. W., Jiang, J.-S., Kuszewski, J., Nilges, M., Pannu, N. S., Read, R. J., Rice, L. M., Simonson, T. & Warren, G. L. (1998). *Acta Cryst.* D**54**, 905–921.
Chao, S. H., Bu, C. H. & Cheung, W. Y. (1995). *Arch. Toxicol.* **69**, 197–203.
Chao, S. H., Suzuki, Y., Zysk, J. R. & Cheung, W. Y. (1984). *Mol. Pharmacol.* **26**, 75–82.
Chin, D. & Means, A. R. (2000). *Trends Cell Biol.* **10**, 322–328.
Chou, J. J., Li, S. P., Klee, C. B. & Bax, A. (2001). *Nature Struct. Biol.* **8**, 990–997.
Evenas, J., Malmendal, A. & Akke, M. (2001). *Structure*, **9**, 185–195.
Fenn, T. D., Ringe, D. & Petsko, G. A. (2003). *J. Appl. Cryst.* **36**, 944–947.
Finn, B. E., Evenas, J., Drakenberg, T., Waltho, J. P., Thulin, E. & Forsen, S. (1995). *Nature Struct. Biol.* **2**, 777–783.
Fullmer, C. S., Edelstein, S. & Wasserman, R. H. (1985). *J. Biol. Chem.* **260**, 6816–6819.
Goering, P. L. (1993). *Neurotoxicology*, **14**, 45–60.
Goldstein, G. W. (1993). *Neurotoxicology*, **14**, 97–102.
Hayward, S. & Berendsen, H. J. C. (1998). *Proteins*, **30**, 144–154.
Hendrickson, W. A. & Lattman, E. E. (1970). *Acta Cryst.* B**26**, 136–143.
Howlin, B., Butler, S. A., Moss, D. S., Harris, G. W. & Driessen, H. P. C. (1993). *J. Appl. Cryst.* **26**, 622–624.
Jones, T. A., Zou, J. Y., Cowan, S. W. & Kjeldgaard, M. (1991). *Acta Cryst.* A**47**, 110–119.
Kuboniwa, H., Tjandra, N., Grzesiek, S., Ren, H., Klee, C. B. & Bax, A. (1995). *Nature Struct. Biol.* **2**, 768–776.
La Fortelle, E. de & Bricogne, G. (1997). *Methods Enzymol.* **276**, 472–494.
Malmendal, A., Evenas, J., Forsen, S. & Akke, M. (1999). *J. Mol. Biol.* **293**, 883–899.
Meador, W. E., Means, A. R. & Quiocho, F. A. (1992). *Science*, **257**, 1251–1255.
Meador, W. E., Means, A. R. & Quiocho, F. A. (1993). *Science*, **262**, 1718–1721.
Merritt, E. A. (1999). *Acta Cryst.* D**55**, 1109–1117.
Murshudov, G. N., Vagin, A. A. & Dodson, E. J. (1997). *Acta Cryst.* D**53**, 240–255.
Olsson, L. L. & Sjolin, L. (2001). *Acta Cryst.* D**57**, 664–669.
Otwinowski, Z. & Minor, W. (1997). *Methods Enzymol.* **276**, 307–326.
Putkey, J. A., Slaughter, G. R. & Means, A. R. (1985). *J. Biol. Chem.* **260**, 4704–4712.

Rice, L. M. & Brünger, A. T. (1994). *Proteins*, **19**, 277–290.
Rosenfield, R. E., Trueblood, K. N. & Dunitz, J. D. (1978). *Acta Cryst.* A**34**, 828–829.
Schomaker, V. & Trueblood, K. (1966). *Acta Cryst.* B**24**, 63–76.
Tjandra, N., Kuboniwa, H., Ren, H. & Bax, A. (1995). *Eur. J. Biochem.* **230**, 1014–1024.
Usón, I. & Sheldrick, G. M. (1999). *Curr. Opin. Struct. Biol.* **9**, 643–648.
Vigil, D., Gallagher, S. C., Trewhella, J. & Garcia, A. E. (2001). *Biophys. J.* **80**, 2082–2092.
Wall, M. E., Clarage, J. B. & Phillips, G. N. (1997). *Structure*, **5**, 1599–1612.
Wilson, M. A. & Brunger, A. T. (2000). *J. Mol. Biol.* **301**, 1237–1256.
Winn, M. D., Isupov, M. N. & Murshudov, G. N. (2001). *Acta Cryst.* D**57**, 122–133.
Zhang, M., Tanaka, T. & Ikura, M. (1995). *Nature Struct. Biol.* **2**, 758–767.